Predictive Capability of WRF Cycling 3DVAR: LiDAR Assimilation at FINO1

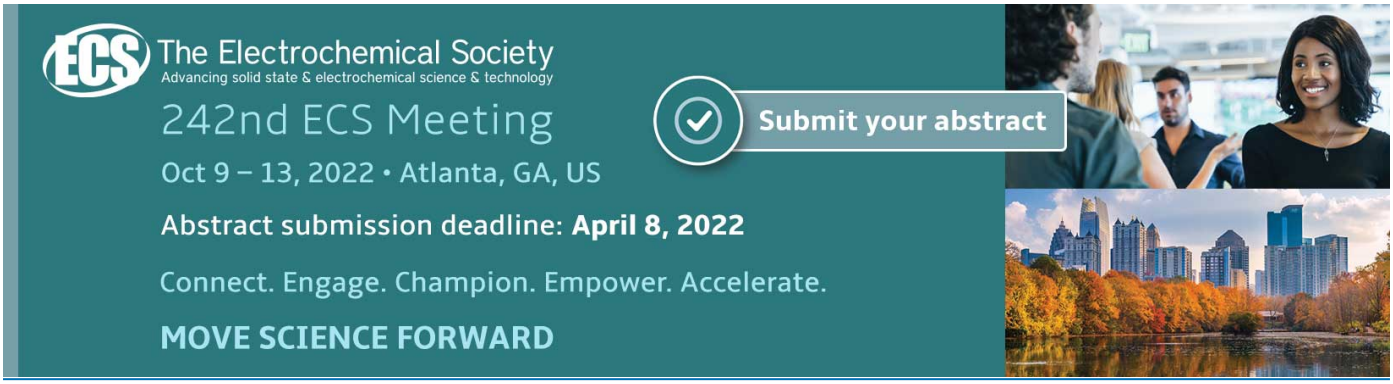

Predictive Capability of WRF Cycling 3DVAR: LiDAR Assimilation at FINO1

Mostafa Bakhoday-Paskyabi and Martin Flügge

Geophysical Institute, University of Bergen, Bergen Offshore Wind Centre, and Bjerknes Centre for Climate Research, Bergen, Norway
NORCE Norwegian Research Centre, Bergen, Norway

E-mail: Mostafa.Bakhoday-Paskyabi@uib.no

Abstract. In this study, we assess tentatively the predictive capability of the Weather Research and Forecasting (WRF) model and its Three-Dimensional Variational (3DVAR) system. We study the impact of LiDAR data assimilation on predictions of wind speed and direction. The simulation domain covers the German wind energy research platform FINO1 in the Southern North Sea, at which the LiDAR data were recorded. The results demonstrate the significance of applying the LiDAR Data Assimilation (DA) with a short assimilation interval (1-hour) to improve the wind prediction and the temporal and spatial representation of low level jet events, compared with an experiment without DA. Furthermore, we briefly examine the impacts of data assimilation cycle length on predictive performance of the DA system, and spatial variability of wind speed over the study area at a height of 250 m.

1. Introduction

The rapid growth in development of large offshore wind projects, consisting of modern wind turbines with heights above 150 m, will establish the wind energy industry as a key player in the worldwide energy market within the next few years. Large turbines operating in regions farther offshore under harsh environmental conditions introduce new technological, technical, and research challenges. For example, our current understanding of atmospheric processes relevant for offshore wind energy applications can be improved by incorporating properly the effects of large scale Marine Atmospheric Boundary Layer (MABL) processes such as land-sea transitions, Low-Level Jets (LLJs) and gravity waves. LLJs over the Southern North Sea have been, however, reported as a common phenomenon [1]. These jets often occur in conjunction with high variable southwesterly winds and have a distinct jet core at heights between 200 m and 300 m. Wind profiles in these heights experience a positive and negative shear below and above the jet core, respectively. The small-scale spatiotemporal variations induced by LLJs modulate turbulence and cause strong impacts on the load characteristics and structural responses of offshore wind turbines [2]. Clusters of wind farms or a large wind park can also affect the structure of LLJs, particularly within the geographical area examined in this study [3]. To reduce the extreme and fatigue loads on large offshore wind turbines, an accurate prediction of LLJs events, i.e. their timings, positions and shapes by the use of measurements and numerical models are highly important.

During the last decade, the use of wind LiDAR's (Light Detection and Ranging) for mapping of the wind field for wind energy applications has become more accepted. LiDAR measurements

with fine temporal and spatial resolutions (e.g. range gate $\leq$ 25 m and frequency up to 0.04 Hz) provide valuable information about LLJs (wind shear and veer). LiDAR data have been recently applied in prediction of LLJ through assimilation into the Numerical Weather Prediction (NWP) models such as Weather Research and Forecasting (WRF) model [4, 5]. In Data Assimilation (DA) techniques, the prognostic variables are updated by quality observations via an optimization framework. Because of the intermittent nature of wind, improvements in wind forecast through DA and other probabilistic models would be important for the power systems [6].

In this study, we use the WRF model to simulate the wind field within the Marine Atmospheric Boundary Layer over the North Sea, covering the geographical area around the German wind energy research platform FINO1 [1]. We aim to tentatively answer following research questions:

- Does a data assimilation based on LiDAR measurements improve the forecasting accuracy of WRF for simulations with approximately coarse horizontal resolutions?
- How large is the impact of the LiDAR data assimilation on predicting processes that take place in the lower part of Marine Atmospheric Boundary Layer (such as LLJs)?

Our main hypothesis is that a WRF model prediction with LiDAR-based DA will improve the one-hourly wind forecast at FINO1 (Section 2), even for a coarse horizontal model resolution. We therefore set up a domain (with horizontal grid-spacing of 9 km) for simulations with and without LiDAR assimilation (Section 3). For data assimilation, we use two estimates of the background error matrix (Section 4) and utilize 10-minute averaged vertical wind profiles up to approximately 1400 m above the mean sea level recorded by a Leosphere Windcube 100s LiDAR system. Additionally, 10-minute averaged wind speed and wind direction recorded at the FINO1 meteorological mast between 33 to 100 m above the mean sea level are utilized for validation purposes. We then quantify tentatively the local and non-local (spatiotemporal) impacts of DA on capturing the LLJ events by applying a regional background error matrix. We finally examine the importance of using two different assimilation cycle lengths in the model forecasts (Section 5).

2. FINO1 platform and observational data

The FINO1 (Forschungsplattformen in Nord und Ostsee, http://www.fino-offshore.de/en) platform is located in the German sector of the North Sea, approximately 45 km off the German Island Borkum in a water depth of approximately 30 m, Fig. 1. The FINO1 platform consists of a 81 m hight meteorological mast that is mounted on the platform's work deck that is located 20 m above the mean sea level. The met-mast is equipped with 8 cup anemometers, 4 wind vanes, 3 sonic anemometers, 3 temperature sensors and 2 pressure sensors. This study utilizes 10-minute averaged cup anemometer and wind vane data collected during July 2015. The measurement height of these instruments is summarized in Table 1. The FINO1 cup anemometer measurements can be expected to be affected by flow distortion effects caused by the met-mast [7, 8]. However, to limit the most severe flow distortion effects, wind coming from directions between $310^{o} \pm 30^{o}$ were omitted from our analyses. The LiDAR data used for assimilation into WRF were collected during the NORCOWE OBLEX-F1 measurement campaign that took place between May 2015 and October 2016 at FINO1. These data were collected with a Leopshre WindCube100s, installed 23 m above the mean sea level, operating in DBS (Doppler Beam Swing) scanning mode. In this scan mode, the LiDAR scanner head elevation angle is fixed at 70^{o} for each of the azimuth angles of 0^{o}, 90^{o}, 180^{o} and 270^{o} (i.e. one round of DBS mode to calculate 3D wind may take about 22 s). We also utilize data from a sonic anemometer that was additionally mounted at 15 m above the mean sea level during OBLEX-F1 measurement campaign. A quality control was performed on both the cup anemometer and the LiDAR data

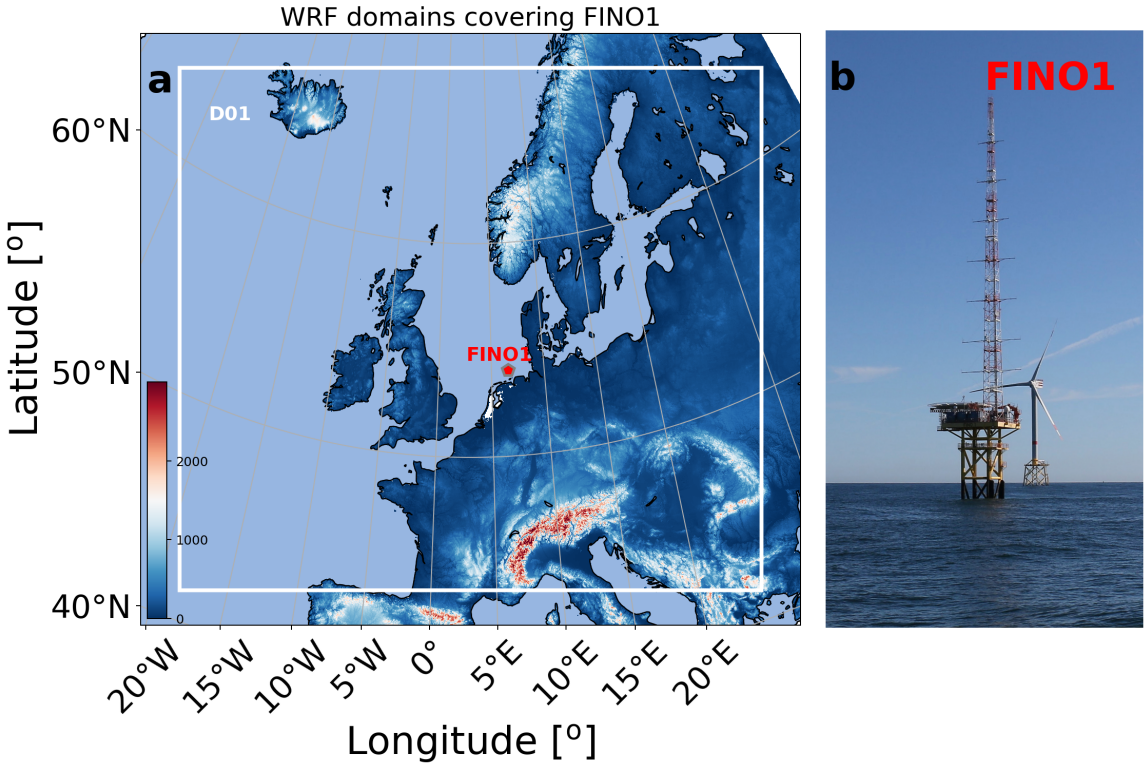

Figure 1. Domain D01 used for the WRF model simulations. All model experiments use horizontal resolution of 9 km, at the North Sea covering the geographic location of FINO1 offshore meteorological mast (red marker, Fig. 1-b). Photo in Fig. 1-b: © NORCOWE/UiB.

Table 1. Observational data sets used in this study.

Instrument	Parameter	Height
Cup anemometer	wind speed	33,40,50,60,70,80,90,100
Wind vane	wind direction	33,50,70,90
LiDAR	wind velocity	75-1400 m every 25 m

to remove outliers and to reject the LiDAR wind speed measurements associated with a Carrier-to-Noise Ratio's (CNR) outside the $[-25, 5]$ dB range. We use 10-min averaged LiDAR DBS measurements for heights between 75 m and 1400 m (depending on data availability).

July 2015 was characterized by several LLJ events which had a wind speed maximum occurring between 200 and 300 m above the mean sea level at FINO1 (Fig. 2-a). A comparison between the (interpolated) LiDAR measurements at 90 m and the corresponding FINO1 cup anemometer wind measurements at the same height is shown in Fig. 2-b. Wind speed time series show very good agreement with a correlation coefficient above $r \geq 93$ (i.e. slop is close to 1) and averaged offset of 1.38 m/s. The time series of wind direction recorded by the (interpolated) LiDAR at 90 m and the FINO1 wind vane at 90 m are shown in Fig. 2-c. Although a volume measurement (LiDAR) is compared with a scalar measurement (wind vane), both time series agree well and have a correlation coefficient above $r \geq 90$ with an average offset of approximately 19° (cf. Fig. 3). In order to gain more insight on atmospheric stability variability during the study period, we categorize the stability conditions into 5 classes based on the high frequency

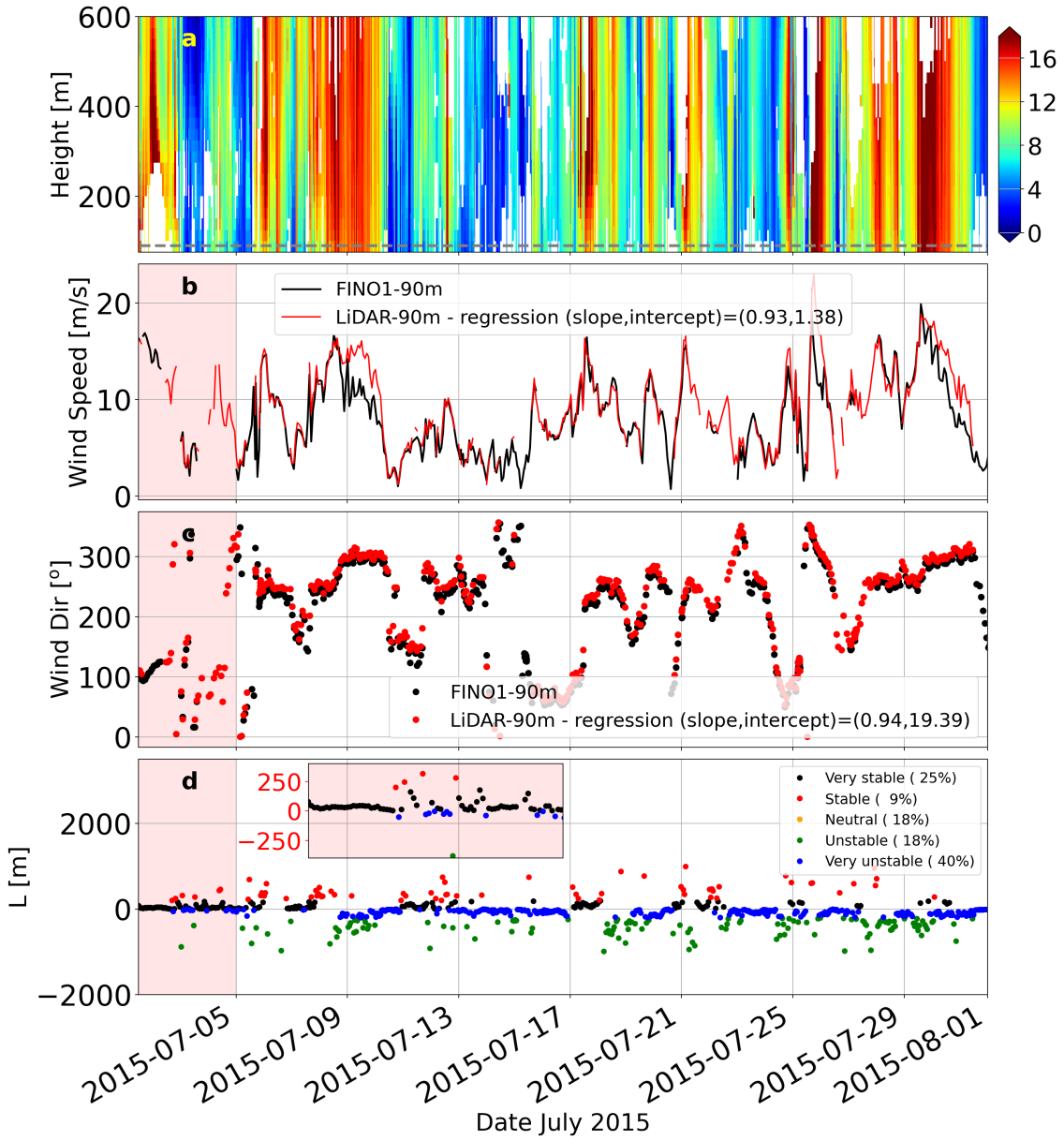

Figure 2. (a) 10-min averaged LiDAR wind speed profiles combined with the met-mast measurements below 100 m for a 5-day period in July 2015; (b) times series comparisons of wind speed at 90 m height measured by FINO1's cup anemometer (black line) and LiDAR (red line) interpolated at 90 m height. Results of regression analysis conducted for these two time series are shown in this figure; (c) times series comparisons of wind direction at 90 m height measured by FINO1's wind vane (black line) and LiDAR (red line). Gray dashed line in Fig. 2-a indicates height of 90 m. Results of regression analysis conducted for these two time series are shown in this figure; and (d) values of the Obukhov length, L, calculated from sonic measurement at height of 15 m above the mean sea level collected with sampling frequency of 25 Hz during July 2015. Five stability classes have been color-coded in this figure along with their respective frequency of occurrence. Shaded red areas highlight the study period between July $1-5$ 2015.

Table 2. Stability classes between 1-5 July 2015.

Stability condition	Range of L	Frequency [%]
Very unstable	$-200 < L \leq 0$	13%
Unstable	$-1000 < L \leq -200$	2%
Neutral	$\|L\| \geq 1000$	0%
Stable	$200 \leq L < 1000$	7%
Very stable	$0 \leq L < 1000$	76%

sonic anemometer data (i.e. 25 Hz) recorded at 15 m above the mean see level. The atmospheric stability (in Fig. 2-d) is derived by means of the Obukhov length L, which is defined as:

$$L = -\frac{u_*^3 \bar{\theta}_v}{\kappa g(\overline{w'\theta'_v})},$$

where g and κ denote the gravitational acceleration and the von Kármán constant, respectively. $\bar{\theta}_v$ indicates the mean virtual potential temperature, and $\overline{w'\theta'_v}$ is the flux of virtual potential temperature, and w' represents the vertical velocity fluctuation. u_* is the friction velocity calculated through the eddy covariance method from sonic velocity measurements. The time series of the atmospheric stability for July 2015 and the study period are shown in Figure 2-d and the corresponding stability classification is given in Table 2.

To provide confidence on reliability of the LiDAR wind profile measurements, we conducted a statistical analysis. Fig. 3 shows the observed Joint Probability Density Function (JPDF), $p(U, V)$, of the meridional and zonal wind components recorded by both the FINO1 cup anemometer at 90 m (i.e. Fig. 3-a) and the LiDAR at 90 m (i.e. Fig. 3-b). Two JPDFs reflect similar positive and negative correlation patterns and variabilty. We observe more pronounced errors at very low wind speeds, e.g. $(U, V) = (0, 0)$. Errors in the wind direction for both very low wind speeds and wind speeds higher than 5 m/s may be responsible for such discrepancies.

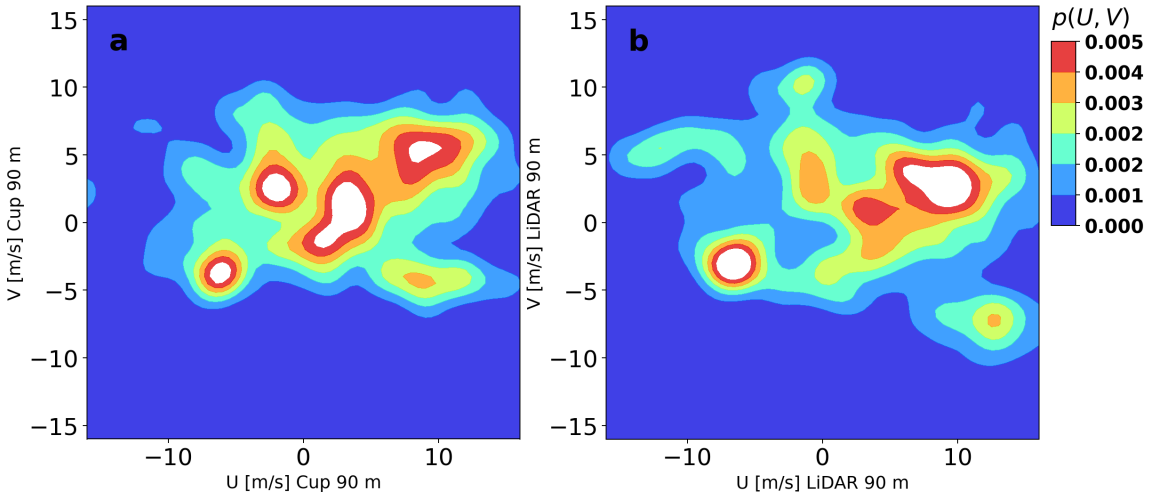

Figure 3. JPDFs of: (a) the zonal; and (b) the meridional wind speeds recorded by the cup anemometer and LiDAR at 90 m height.

3. Model setup

The mesoscale atmospheric model WRF-ARW V4 was set up for a single domain (i.e. 401×301 grid points) with a horizontal resolution of 9 km around the FINO1 platform, covering properly the Southern North Sea (c.f. Fig. 1). We used 53 vertical η-levels with higher resolution towards the surface (i.e. 22 vertical levels below 300 m) and lower resolution at higher altitudes, as well as four soil levels. The model's air pressure at the upper level was set to 50 hPa. We select the Yonsei University (YSU) PBL scheme (i.e. bl_pbl_physics=1). Operational global reanalysis data from ERA5 are used for the model initial and lateral boundary conditions. WRF runs with three experiments are conducted for the time period between 1 and 5 July 2015, where the LiDAR has recorded a couple of strong LLJ events, namely: run with DA using the global background error matrix (WRFDA-GLOBE), DA experiment using a regional background error matrix (WRFDA-REGBE), and run without DA (WRF-NODA). Two DA-based experiments are done in cycling mode with a one-hour assimilation cycle length. We use a 12h spin-up prior to the actual model run, and the first guess for DA experiments is provided by WRF output after spin-up. The regional background error covariance is estimated using the National Meteorological Center (NMC) method (see Section 4). In this study, control variables for DA are horizontal wind speed and wind direction from only the LiDAR measurements. In our analyses, we take the nearest grid point of the WRF model output close to the FINO1 geographical location (i.e. at 54.0148618N, 6.5876398E).

4. 3DVAR algorithm

The 3DVAR assimilation framework in WRF combines the background field information and observational data by the use of a statistically optimal estimation [9, 13] that minimizes the following cost function:

$$J(\boldsymbol{x}) = \frac{1}{2}(\boldsymbol{x} - \boldsymbol{x}^b)^T \boldsymbol{B}^{-1}(\boldsymbol{x} - \boldsymbol{x}^b) + \frac{1}{2}(\boldsymbol{y} - \boldsymbol{y}^o)^T \boldsymbol{R}^{-1}(\boldsymbol{y} - \boldsymbol{y}^o), \tag{1}$$

where the vector $\boldsymbol{x}$ denotes the analysis field, $\boldsymbol{x}_b$ is the background state vector, $\boldsymbol{y}$ represents the observation vector, $\boldsymbol{B}$ is the background error covariance matrix, and $\boldsymbol{R}$ indicates observation error covariance matrix that becomes diagonal by assuming there is no correlation between different instruments and measurements performed by the same instruments. $\boldsymbol{y}^o = \boldsymbol{H}(\boldsymbol{x})$ is the same as the vector $\boldsymbol{y}$ in which $\boldsymbol{H}$ transforms the model variables $\boldsymbol{x}$ into the observation space (e.g. a linear operator interpolating the values from model 3D grids to observational points). The 3DVAR DA looks then for a solution to minimize the cost function in Eq. (1).

Estimating the background error covariance matrix $\boldsymbol{B}$ introduced in Eq. (1) as correctly as possible (computationally very costly) is of uttermost importance because it controls the expansion of corrections in the model based on information provided from assimilated measurements and it determines the weights of the background information and observations across the forecast fields [10]. In this study, we use a relatively computationally economic NMC statistical approach to calculate $\boldsymbol{B}$ for wind data [11]. The algorithm consists of the following stages: (1) it removes the mean from the control variables (and then binning) to estimate the corresponding perturbations; (2) it estimates the covariance errors between different control variables; and (3) it calculates the horizontal length scales. In order to use the algorithm in this study, we utilize the differences between 12h and 24h forecasts valid at the same timestamp for just 8 days ahead. These two short-term forecasts create a database of pair forecasts corresponding to certain hours of day. The key assumption is that the statistical properties of the actual $\boldsymbol{B}$ appearing in Eq. (1) is the same as the differences between the forecasts belonging to each pair. The estimate of $\boldsymbol{B}$ in the NMC sense is then given as follows:

$$\boldsymbol{B} = \overline{(\boldsymbol{x}_b^{24h} - \boldsymbol{x}_b^{12h})(\boldsymbol{x}_b^{24h} - \boldsymbol{x}_b^{12h})^T}, \tag{2}$$

where $\boldsymbol{x}_b^{12h}$ and $\boldsymbol{x}_b^{24h}$ denote the state of atmosphere predicted from the pair forecasts with 12h and 24h intervals respectively. The overbar represents an average over both time and space. It is noted that using only a few days of forecasts will generate only a few pairs to be used in the NMC procedure. While these few pairs are still appropriate for our purpose, but they are generally insufficient to statistically capture important features of the original background error covariance matrix.

5. Results

We convert the LiDAR measurements into 'little_r' data format [12] and discard timestamps and heights where no LiDAR data are available. For altitudes above the LiDAR data availability (approximately above 1400 m here), simulations are least affected by DA (i.e. WRFDA simulations are almost the same as WRF-NODA results). Several local phenomena cannot be captured and are smoothed out from our WRF simulations due to the spatial resolution of 9 km. We apply 3DVAR every 1 hour in a cycling mode, and the forecast lead time represents the end of the 1-hour cycle. The temporal and spatial resolution discrepancies of LiDAR measurements and WRF simulations may influence the performance of the DA that is not addressed in this study. Note that the deceleration of the wind speed due to the wind farms located in the vicinity of the FINO1 and inside the model domain has not been considered in all simulations.

In Fig. 4, we show some properties of the background error covariance matrix $\boldsymbol{B}$ used in the WRFDA-REGBE experiment, including the first five eigenvectors of the stream function, the unbalanced part of the velocity potential and the unbalanced part of the temperature variables. These eigenvectors are estimated from the Empirical Orthogonal Function (EOF) analysis of the vertical auto-covariance matrix to calculate, for example, the length scales as shown in Figs. 4e,f, and h. The horizontal length scales describe the spread of observational information. For 9 km horizontal resolution, values of length scales for the stream function and unbalance velocity potential are approximately around $200 - 250$ km for the first EOF mode. However, the length scale of temperature shows smaller value about 35 km for the first EOF mode. If we use more forecast pairs in generation of the regional $\boldsymbol{B}$, all length scales should decrease to about grid spacing at higher EOF modes (i.e. a small radius of influence).

We compare between the wind speed measurements and the WRF simulations for altitudes below 550 m with and without DA in Fig. 5. Data from all simulations are extracted at the WRF model grid point nearest to the FINO1 geographical location. The horizontal wind speed observed at FINO1 during our study period between July 1–5 is shown in Fig. 5-a. Three LLJs events are clearly seen in this panel, one long LLJ event lasting between July 1–2, and two short transient LLJ events at the afternoon of July 2 and around July 3 00UTC. A fourth (weak) LLJ event appears to have occurred at noon on July 4, however most of the observational LiDAR data are lacking at this time period. The fifth event occurs at afternoon on July 5. The best agreement between the WRF simulations and the LiDAR observations is reached for both WRFDA simulations in terms of statistical diagnostics such as the mean difference, the wind speed vertical distribution and the root mean square error. The WRF-NODA model overestimates the wind speeds during almost all events (which occurred during very stable atmospheric condition, sea Fig. 2-d). This is, however, to be expected when the effects of wind farms are not accounted for in all simulations, particularly WRF-NODA experiment. Wind speeds from the WRFDA-GLOBE simulation provides better agreement with LiDAR observations than the WRF-NODA output at heights below 550 m. It is evident that the WRF-NODA simulation is unable to capture the time, location, and shape of the second and the third LLJ event on the afternoon of July 2 and at around July 3 00UTC. In contrast, these two LLJ events are clearly visible in the WRFDA results. We notice that all WRF simulations captured the forth event that occurred at noon on July 4, and WRF-NODA and WRFDA-REGBE predict the fifth event by shifting the time of its occurrence for about couple of minutes to few hours. It

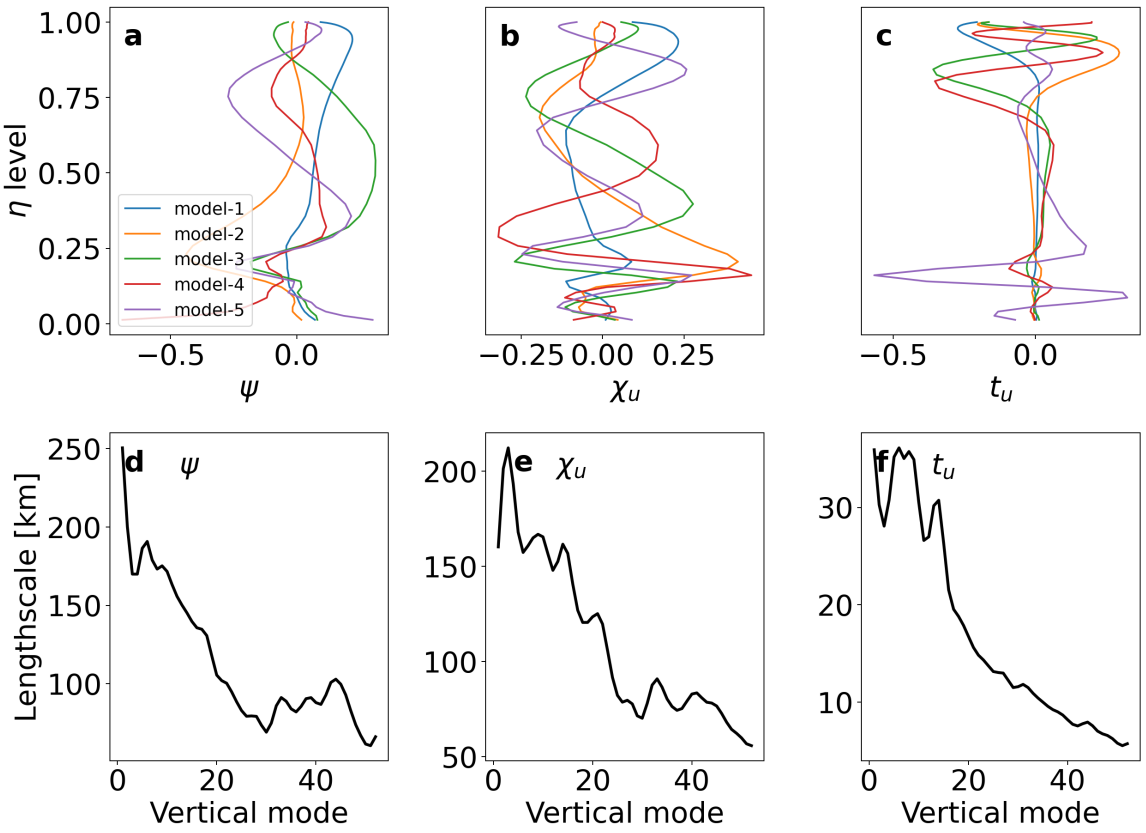

Figure 4. (a,b,c) Five eigenvectors of stream function, ψ, unbalanced part of velocity potential, χ_u, and the unbalanced part temperature, t_u, for all vertical levels. The eigenvectors are estimated from EOF decomposition of the vertical autocovariance matrix; and (d,e,f) horizontal length scales of leading EOF modes of the background error covariances for stream functions, velocity, and temperature respectively.

is noted that in the WRFDA simulations, the difference in wind speed does not approach zero because the results have been interpolated to the nearest grid cell at the geographical location of FINO1. The simulations in Fig. 5 are presented for altitudes below 550 m, where the LiDAR measurements had the highest data availability.

As the simulation accuracy for the u and v wind vector components might differ, we also investigate the effects of LiDAR DA on the modelled wind direction. Figure 6 shows that wind direction from the WRF-NODA experiment indicates a significant difference with respect to the LiDAR observations around July 3 00UTC (at all levels below 550 m). In general, both WRFDA experiments could capture fairly well the variation of wind direction, especially during the first 24 hours of simulations. We notice that the WRF-NODA and the WRFDA outputs also provide a fairly good agreement between wind direction estimates and LiDAR observations (mainly during stable conditions followed by an unexpected behaviour during unstable condition).

Figure 7-a and b show comparisons of hourly horizontal wind directions and speeds from all model experiments against observed LiDAR data at an altitude of 250 m. While the WRF model systematically performs well in all experiments, the WRF-NODA reveals the largest biases against observations, particularly during July 3 after the first few LLJ events, as highlighted by the colored areas. This period is characterized by a good LiDAR data availability and the WRFDA-GLOBE model run could perform a slightly better prediction of the wind field.

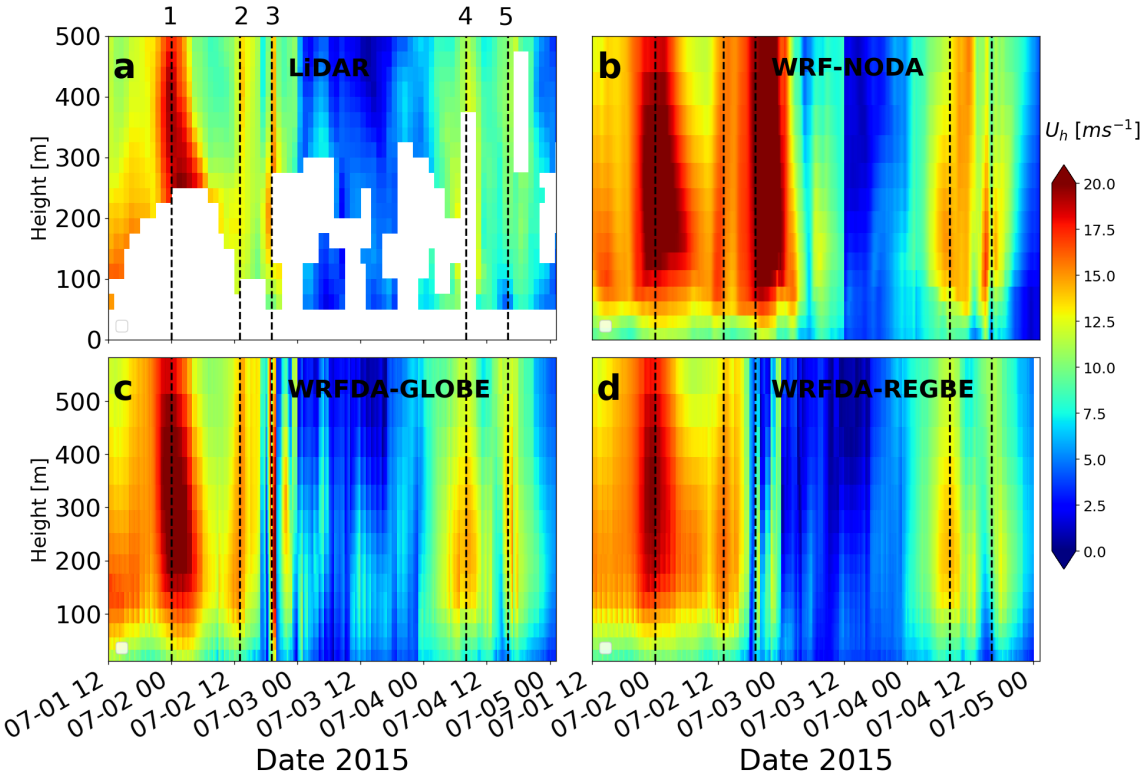

Figure 5. Representation of observed and modeled horizontal wind speeds at FINO1 over the study period July 1–5 2015: (a) LiDAR measurement. Vertical dashed lines show the first three LLJ events; (b) WRF without DA; (c) WRF with DA using the regional BE matrix (i.e. WRFDA-REGBE); and (d) WRF with DA using the global BE matrix (i.e. WRFDA-GLOBE). The white spaces in the LiDAR plot corresponds to the filtered data due to insufficient data quality or none-availability of data.

However, both WRFDA experiments overestimate the wind speeds during wind period between July 1 and July 3, most likely due to the insufficient LiDAR data availability over this period at heights below 400 m, or the need for longer model spin-up time (see Fig. 5-b). The Taylor diagram in Fig. 7-c provides a more comprehensive statistical comparisons between the WRF model experiments and the observed wind speeds for the time series shown in Fig. 7-b. While the accuracy levels are quite promising for all experiments, the WRFDA results exhibit a larger correlation coefficient accompanied by a lower standard deviation. Therefore, we conclude that the DA simulations could effectively decrease the error with respect to the wind speed measurement. Figure 7-d shows the corresponding statistical comparison between the observed and modelled wind directions at an altitude of 250 m. All three experiments exhibit very similar statistics, and results highlight the low performance of WRF-NODA in capturing properly the wind direction variability after the first 24-hour.

Figure 8-a shows the LiDAR-measured wind speed variation for times between July 1 18UTC to July 3 00UTC (after the first few LLJ events). Averaged wind profile over this time period in Fig. 8-b shows that the assimilated experiments are closer to the averaged observed wind speed profile (asterisk red markers). In particular, the WRF-NODA significantly overestimates the wind speed at heights where LiDAR data is available. It is evident that WRFDA-GLOBE leads better agreement than other experiments by appropriately representing the wind speed and its shear at heights above 250 m. Furthermore, the height of maximum wind speed (height of the

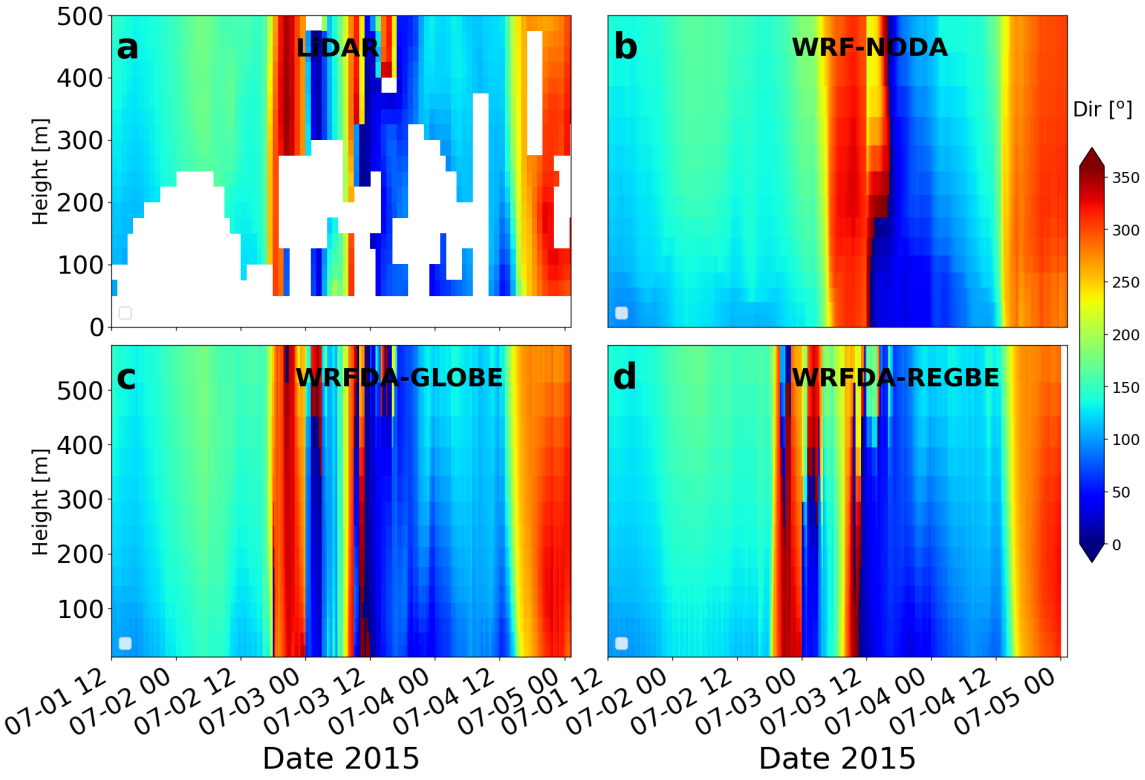

Figure 6. Representation of measured and modeled wind directions at FINO1 over the study period July 1–5: (a) LiDAR measurement. Vertical dashed lines show the first three LLJ events; (b) WRF without DA; (c) WRF with DA using the regional BE matrix (i.e. WRFDA-REGBE); and (d) WRF with DA using the global BE matrix (i.e. WRFDA-GLOBE).

jet core) shifts from about 193 m for the WRFDA simulations to about 224 m for the WRF-NODA run. Figure 8-c shows the available LiDAR-measured wind direction during the same period. The 10-min mean wind direction profiles averaged over this period are demonstrated in Fig. 8-d. The profile of WRF-NODA experiment (red line) deviates significantly from the available LiDAR measurements (red markers). The discrepancies between WRFDA-REGBE and WRFDA-GLOBE increase by height, where the accuracy of WRFDA-REGBE declines. In general, including DA in simulations leads to an overall better wind speed and direction predictions during this time interval.

LiDAR-based DA has been based on LiDAR wind and direction data for heights above 75 m. To further evaluate the performance of DA with respect to prediction of the wind speed, we conduct a comparison between all WRF experiments and available cup measurements at 70 m and 40 m heights, where LiDAR data were not available for DA. Figure 9 shows the WRF predictive skill is significantly enhanced when using DA at both heights, particularly DA experiments. It is noted that we postpone more comprehensive statistical analysis in another work.

Figure 10 displays an example on how applying the LiDAR DA in the WRF experiment affects the spatial variability of the modelled wind speed at 250 m height at July 2 12UTC. The model results of WRF-NODA (Fig. 10-a) and WRFDA-GLOBE (Fig. 10-b) show a very similar spatial variability of wind speeds. It is evident that the results of the two simulations are not exactly identical in regions away from the FINO1. For a single-point DA, one would expect that the largest discrepancies between the two simulations only occur in regions around the FINO1

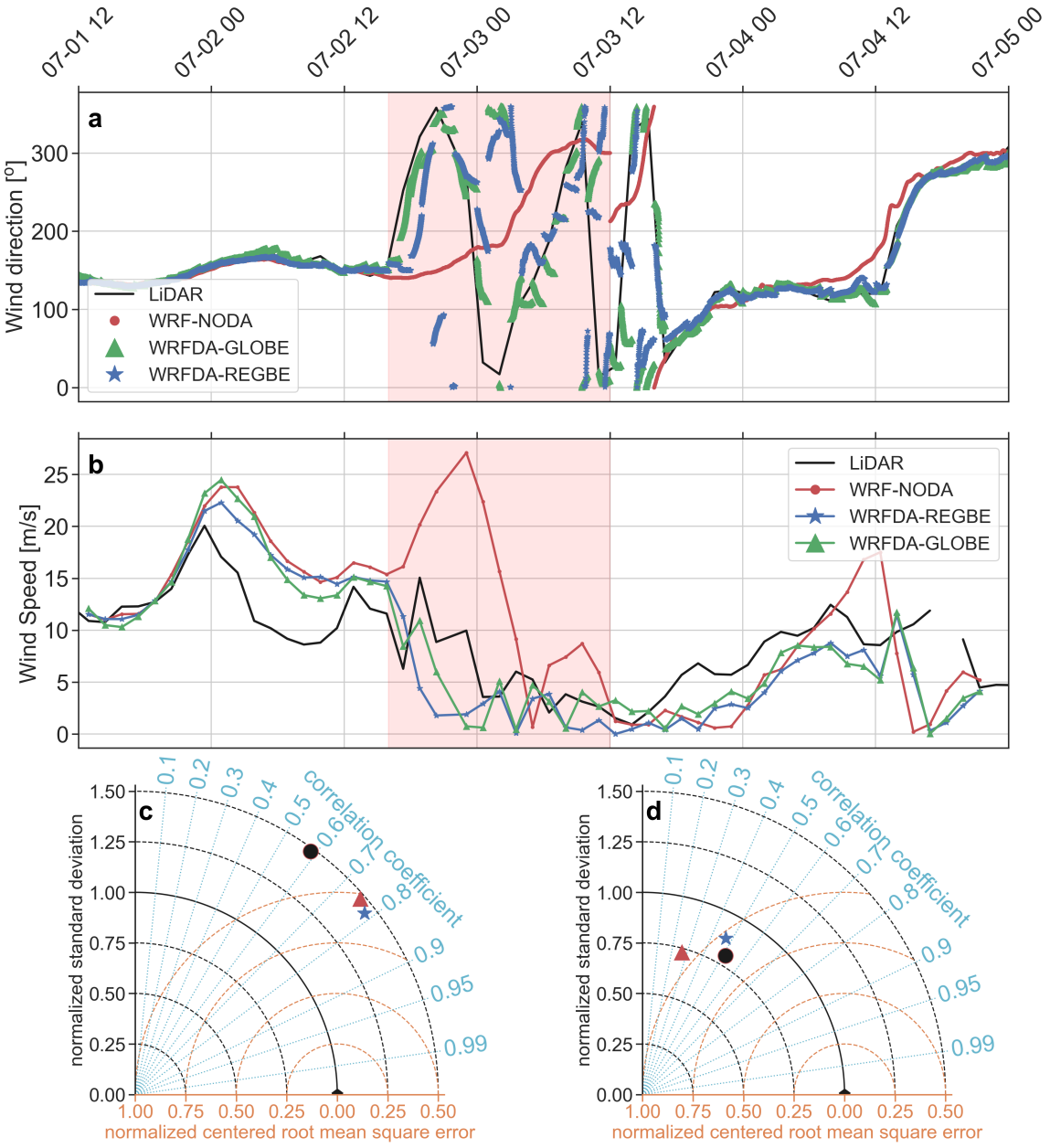

Figure 7. (a) Comparison of hourly wind speeds at 250 m from the three model experiments with respect to the observed LiDAR data at the same height; (b) time series of wind directions from three model experiments against LiDAR data at the same height; and (c,d) Taylor Diagram to compare the three model time series of wind direction (a) and wind speed (b) at 250 m height and the corresponding observed data in terms of Centered Root Mean Square Error, Correlation Coefficient, and Standard Deviation. Markers stands for WRFDA-REGBE (red triangle), WRFDA-GLOBE (blue asterisk), and WRF-NODA (black circle).

where the DA explicitly affects the model state and its variability within a radius of influence containing the FINO1 (e.g. see the length scales of regional $\boldsymbol{B}$ in Fig. 4 that define the radius of influence associated with observations). Furthermore, WRFDA experiments in Figs. 10-b and 10-c show a more smooth wind speed for almost entire domain compared with WRF-NODA.

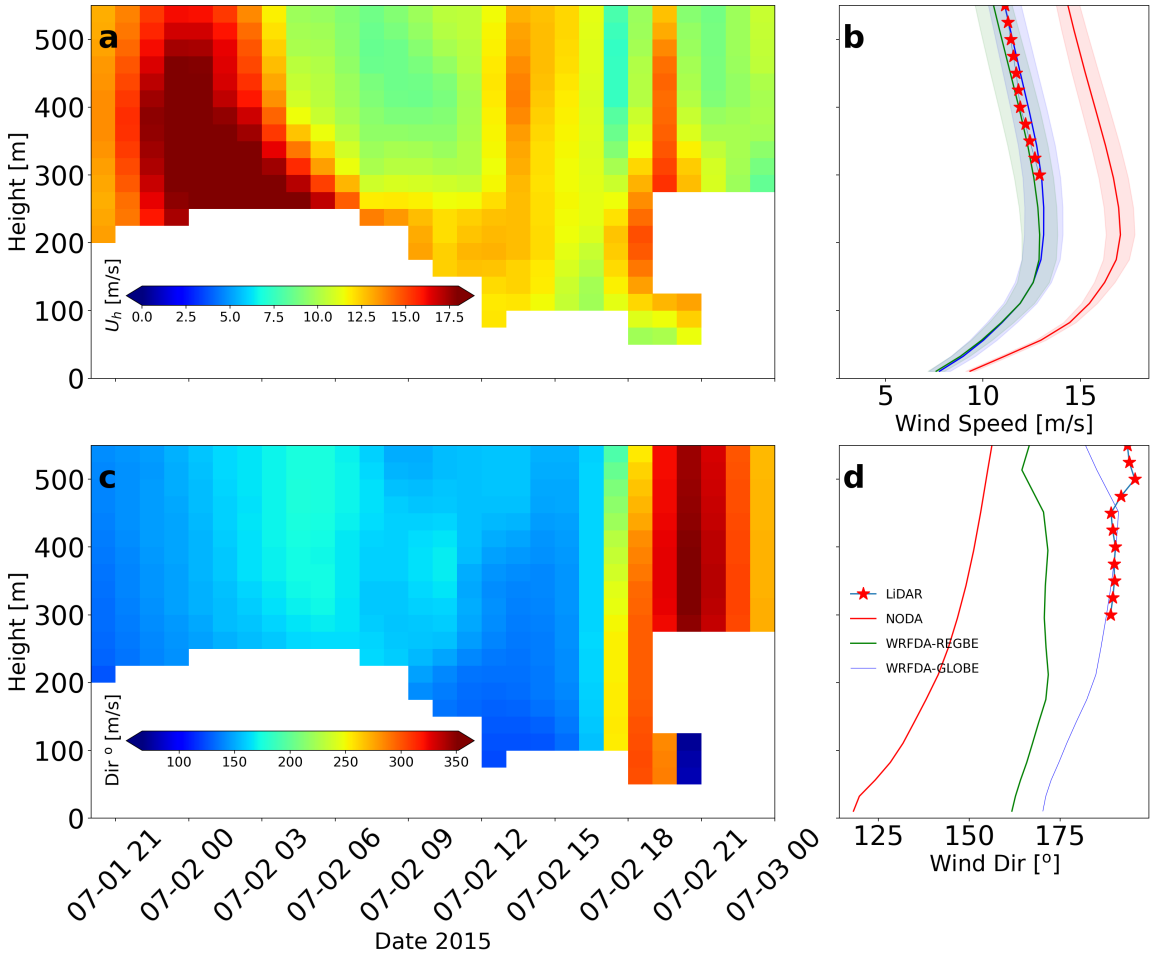

Figure 8. Mean wind speed profiles averaged temporally between 2015-07-02_12:00 and 2015-07-02_06:00 at heights less than 700 m for WRF-NODA (red line), WRFDA-GLOBE (gray line), WRFDA-REGBE (black dashed line), and available LiDAR measurements (red markers).

Why does the influence of the DA at a single-point spread out over a wide areas even away from the FINO1 location? Is there a mismatch between the dynamical scales resolved by the observation and DA predicting system? To answer these questions we conducted an experiment to study whether the growth of model error in the area away from the FINO1 depends on the forecast cycle length. We increased the forecast cycle length from 1h to 6h (i.e. Fig. 10-d). It is observed that the 6h DA cycle system delivers a reliable wind field (see the wind fields inside the red boxes as shown in Fig. 10), particularly for regions away from FINO1 that we do not expect any distinguishable modification of flow field by our single-point DA systems. Furthermore, the wind speed is no longer that smooth containing more pronounced small-scale features compared with Figs. 10-b and c. The 6h cycle length reveals a good memory from observations in the area of influence around the FINO1 platform. Studying the characteristics of such errors and remained smoothed features in the 6h cycle system are tackled elsewhere.

To further understand the differences between different simulations, we indicate the horizontal velocity at 2nd July 2015 for a cross section shown in Fig. 11-a, red line. The cross section extends from south to north (i.e. a line of constant longitude at 6°) over the Southern North Sea close to the FINO1 platform. While all numerical experiments share similar structures near

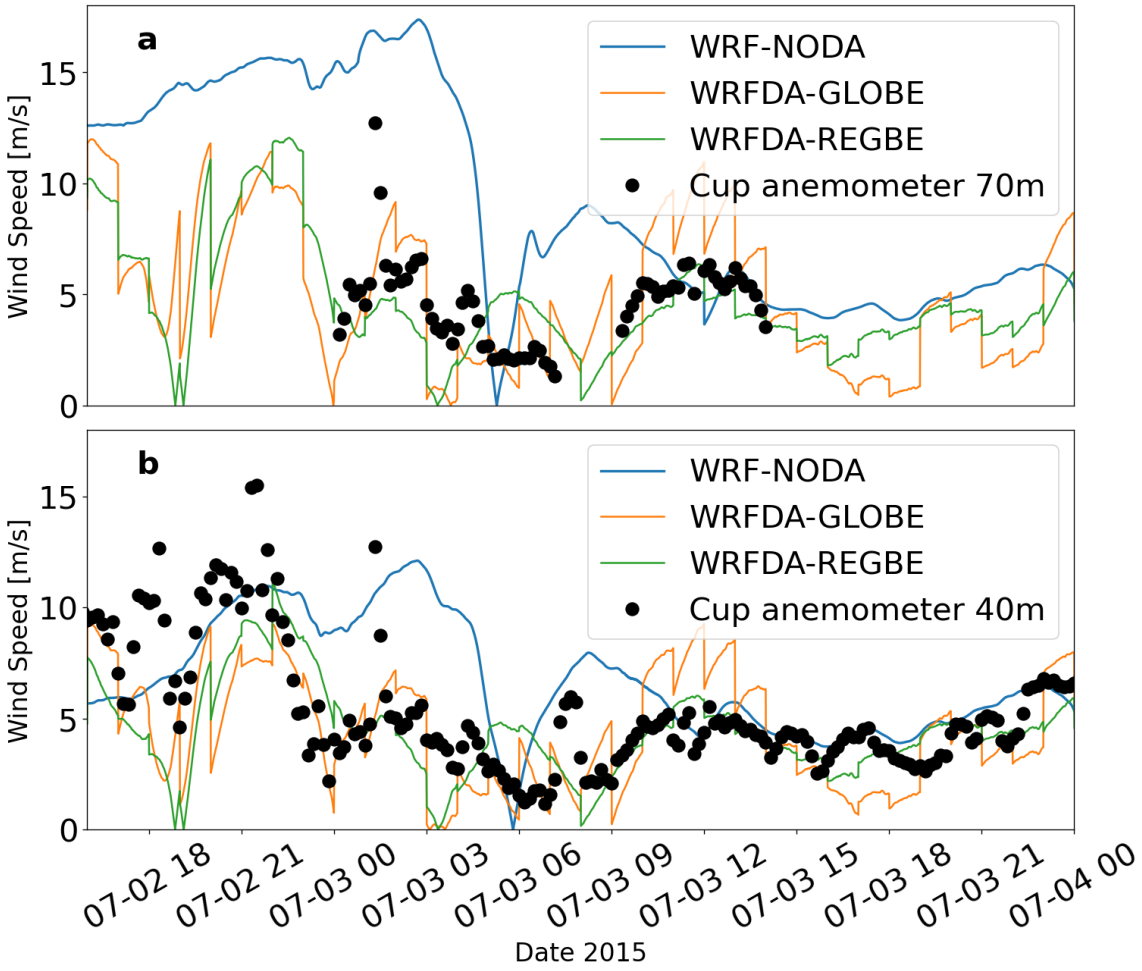

Figure 9. Time series of wind speeds from different WRF experiments against available cup anemometer measurements at two heights: (a) 70 m; and (b) 40 m.

the surface, the WRF-NODA simulation (i.e. Fig. 11-b) shows very intensified wind speed with slightly different vertical distribution compared with the LiDAR-based assimilation results (i.e. Figs. 11-c and d). The differences are largest for heights between 120 m and 380 m and decrease at higher altitudes. It is further observed that the wind speeds in latitudes close to the study site experience, somewhat, the largest changes (see the length scales of the DA influencing radius in Fig. 4-d, e, and f).

6. Conclusions

In this study, we have shown how an approximately coarse WRF model forecast (i.e. 9 km horizontal resolution) can be improved by assimilation of LiDAR data. For the variational DA, we used two different types of background error matrices $\boldsymbol{B}$ (i.e. global and regional) and studied how they could improve the predictions of the wind field by relying on the differences between the forecasted and observed variables. While using the regional estimate of $\boldsymbol{B}$, i.e. REGBE, provided good agreement with respect to the LiDAR observations and measurements from cup anemometers, a more comprehensive assessment is required in order to cover a wide range of non-local and local processes, in addition to using various assimilation intervals for the DA experiments. Furthermore, we used very few pairs of forecasts (i.e. for 8 days in July 2015)

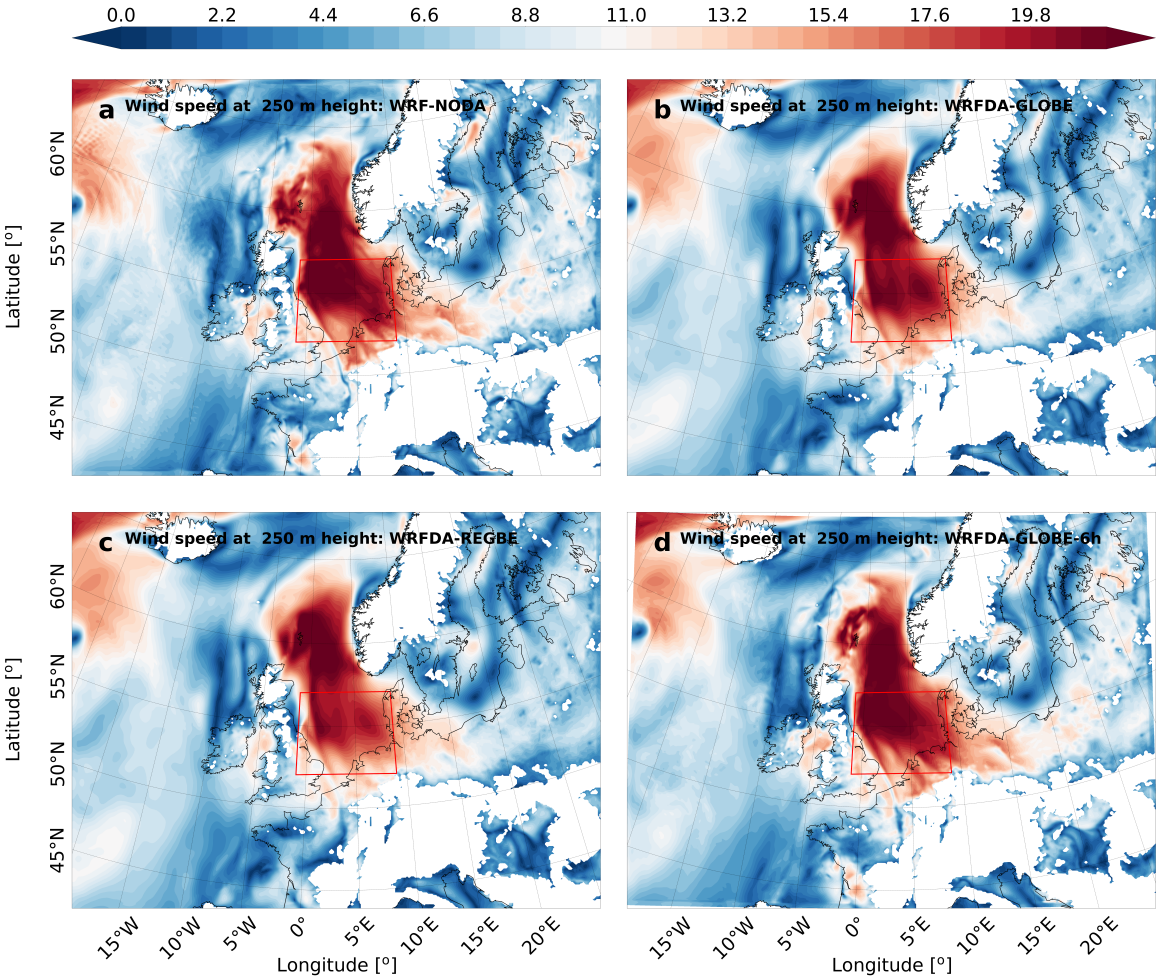

Figure 10. Examples of 250 m instantaneous wind speed maps at July 2 12UTC for four WRF experiments: (a) WRFDA-NODA; (b) WRFDA-GLOBE with 1-hour forecast cycle length; (c) WRFDA-REGBE with 1-hour forecast cycle length; and (d) WRFDA with global error covariance matrix and a forecast cycle length of 6-hour.

to estimate the background error. How the selection of this short duration and the number of created pairs affect the uncertainty of the $\boldsymbol{B}$-estimation was not explored here.

LiDAR data for assimilation were provided for altitudes above 75 m. We hence compared the DA simulation results to cup anemometer records for heights where no data from LiDAR was available for assimilation system (i.e. heights of 40 m and 70 m). Tentative comparisons at these two heights confirmed that DA can deliver reliable forecasts at heights close to the surface.

We briefly examined the spatial impacts of the forecast cycle length, and compared results of using two different cycle lengths: 1-hour and 6-hour. For wind speed field at 250 m height, it turned out that 6-hour cycle system reduces spatial impacts of observations on the forecast particularly in regions away from the study site. We have not studied how the 6-hour cycle system improves predictability of models compared with the 1-hour cycle model experiments for the entire study period.

Our analyses are tentative based on a coarse model configuration without nesting. The sensitivity of DA impacts on the multiple nesting experiments as well as spin-up time interval will be further investigated in other independent studies.

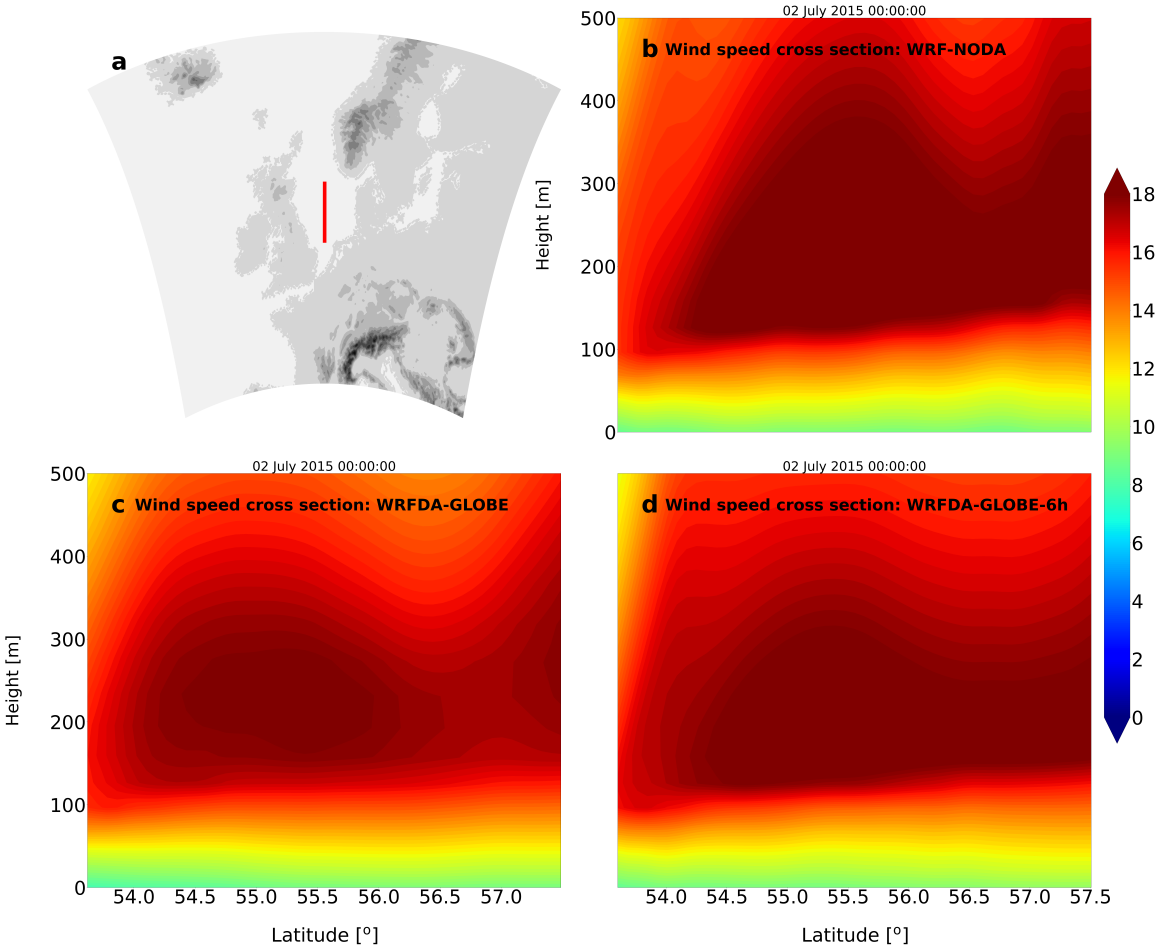

Figure 11. South-north cross-sections of wind speeds from different WRF experiments at July 2 00UTC: (a) map of study area and cross-section line (red line); (b,c,d) wind speeds from WRF-NODA, WRFDA-GLOBE, and WRFDA-REGBE respectively. All WRFDA results are based on 1h cycle setting.

7. Acknowledgment

This work was supported by the Research Council of Norway through Research cooperation with China on energy, ENERGIX, grant number 304229. The full title of project 304229 is "CONWIND: Research on smart operation control technologies for offshore wind farms". The simulations were performed on resources provided by UNINETT Sigma2 - the National Infrastructure for High Performance Computing and Data Storage in Norway. The Lidar data used in this study were gathered as part of the OBLEX-F1 field campaign that has been performed under the Norwegian Centre for Offshore Wind Energy (NORCOWE) funded by the Research Council of Norway (RCN 193821), the Offshore Boundary Layer Observatory (OBLO) project (project no. RCN 227777) and the Norwegian e-infrastructure NorStore (project no. RCN: NS9060K). OBLEX-F1 was coordinated in collaboration between the University of Bergen (Geophysical Institute) and NORCE Norwegian Research Centre (project executing organization). The Federal Maritime and Hydrographic Agency of Germany (BSH) is acknowledged for providing the FINO1 reference data through the FINO database at http://fino.bshde/. The FINO project (research platforms in the North Sea and Baltic Sea) is funded by the BMU, the German Federal Ministry for the Environment, Nature Conservation,

Building and Nuclear Safety in collaboration with Project Management Jülich GmbH (project no. 0325321). The FINO1 meteorological reference data were provided by Deutsches Windenergi Institut (DEWI). We also thank the FINO1 platform operator Forschungs- und Entwicklungszentrum Fachhochschule Kiel GmbH (FuE Kiel GmbH) for their support (project no. 0329905E).

References

[1] Wagner, D., Steifeld, G., Witha, B., Wurps, H., and Reuder, J., 2019 Low Level Jets over the Southern North Sea, *Meteorol. Z.*, 28, 389–415.
[2] Gutierrez, W., Ruiz-Columbie, A., Tutkun., M., Castillo, L., 2017 Impacts of the low-level jet's negative wind shear on the wind turbine, *Wind Energ. Sci.*,2, 533–545, DOI: 10.5194/ wes-2-533-2017.
[3] Larsén, X.G. and Fischereit, J., 2020 A case study of wind farm effects using two wake parameterizations in WRF (V3.7) in the presence of low level jets, *Geoscience Model Development: Discussions*, 14, 3141–3158.
[4] Lee, J.C. and Lundquist, J.K., 2017 Evaluation of the wind farm parameterization in the Weather Research and Forecasting model (version 3.8.1) with meteorological and turbine power data, *Geoscientific Model Development*, 10, https://doi.org/10.5194/gmd-10-4229-2017.
[5] Nunalee, C.G. and Basu, S., 2014 Mesoscale modeling of coastal low-level jets: Implications for offshore wind resource estimation, *Wind Energy*, 17, 1199–1216.
[6] Collins, J., Parkes, J., and Tindal, A., 2009 Short Term Forecasting for Utility-Scale Wind Farms-The Power Model Challenge,*Wind Engineering*, 3, 247–257.
[7] Neumann, T., Mittelstaedt, E., Gerasch, W.J., and Fischer, G., 2003 Erection of German offshore measuring platform in the North Sea, *DEWI Magazin*, 23, 32–46.
[8] Neumann, T., and Nolopp, K., 2007 Three years operation of far offshore measurements at FINO1, *DEWI Mag*, 30, 42–46.
[9] Barker, D., Huang, W., Guo, Y.R., Bourgeois, A., 2019 A Three-Demiensional Variational (3DVAR) Data Assimilation System for Use with MM5 (*No. NCAR/TN-453+STR)*, Available online: https://opensky.ucar.edu/islandora/ object/technotes%3A309.
[10] Derber, J. and Bouttier, F., 1999 A reformulation of the background error covariance in the ECMWF global data assimilation system, *Tellus*, 51A, 195–221.
[11] Parrish, D.F. and Derber, J.C., 1992 The National Meteorological Center's spectral statistical interpolation analysis system, *Mon. Weather Rev.*, 120, 1747–1763.
[12] Dudhia, J., 2005 The Weather Research and Forecast Model Version 2.0: Physics Update, *WRF/MM5 User's Workshop*, http://www2.mmm.ucar.edu/mm5/workshop/ws04/Session1/Dudhia.Jimy2.pdf.
[13] Courtier, P., Thépaut, J.N., and Hollingsworth, A., 1994 A strategy for operational implementation of 4D-Var, using an incremental approach, *Q. J. Roy. Meteor. Soc.*, 120, 1367–1387.